

# Toward a Visible Light-Driven Photocatalyst: The Effect of Midgap-States-Induced Energy Gap of Undoped TiO<sub>2</sub> Nanoparticles

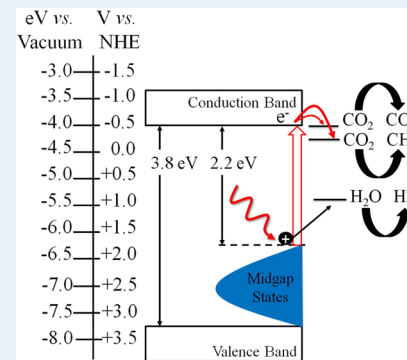
Houman Yaghoubi,<sup>\*,†,‡,§</sup> Zhi Li,<sup>||</sup> Yao Chen,<sup>‡</sup> Huong T. Ngo,<sup>†</sup> Venkat R. Bhethanabotla,<sup>†</sup> Babu Joseph,<sup>†</sup> Shengqian Ma,<sup>‡</sup> Rudy Schlaf,<sup>||</sup> and Arash Takshi<sup>†</sup>

<sup>†</sup>Bio/Organic Electronics Lab, Department of Electrical Engineering, <sup>‡</sup>Department of Chemistry, <sup>§</sup>Nanotechnology Research and Education Center, <sup>||</sup>Surface Science Lab, Department of Electrical Engineering, <sup>†</sup>Department of Chemical and Biomedical Engineering, University of South Florida, Tampa, Florida 33620, United States

## Supporting Information

**ABSTRACT:** TiO<sub>2</sub> is one of the most promising candidate materials for clean-energy generation and environmental remediation. However, the larger-than 3.1 eV bandgap of perfectly crystalline TiO<sub>2</sub> confines its application to the ultraviolet (UV) range. In this study, the electronic and the optical properties of undoped mixed-phase TiO<sub>2</sub> nanoparticles were investigated using UV and inverse photoemission, low intensity X-ray photoelectron (XP), and diffused reflectance spectroscopy methods. The facile solution-phase synthesized nanoparticles exhibited a midgap-states-induced energy gap of only ~2.2 eV. The diffused reflectance spectrum showed sub-bandgap absorption due to the existence of a large Urbach tail at 2.2 eV. The UV photoemission spectrum evidenced the presence of midgap states. The 2.2 eV energy gap enables the nanoparticles to be photoactive in the visible energy range. The gas-phase CO<sub>2</sub> photoreduction test with water vapor under visible light illumination was studied in the presence of the synthesized TiO<sub>2</sub> nanoparticles which resulted in the production of ~1357 ppm gr<sup>-1</sup><sub>(catalyst)</sub> CO and ~360 ppm gr<sup>-1</sup><sub>(catalyst)</sub> CH<sub>4</sub>, as compared to negligible amounts using a standard TiO<sub>2</sub> (P25) sample. The synthesized nanoparticles possessed a Brunauer–Emmett–Teller (BET) surface area of ~131 m<sup>2</sup> gr<sup>-1</sup>, corresponding to a Langmuir surface area of ~166 m<sup>2</sup> gr<sup>-1</sup>. The determined interplanar distances of atomic planes by high-resolution transmission electron microscopy (HR-TEM) and X-ray diffraction (XRD) methods were consistent. A detailed elemental analysis using XPS and inductively coupled plasma mass spectrometry (ICP-MS) demonstrated that the synthesized catalyst is indeed undoped. The catalytic activity of the undoped synthesized nanoparticles in the visible spectrum can be ascribed to the unique electronic structure due to the presence of oxygen vacancy related defects and the high surface area.

**KEYWORDS:** visible light photocatalyst, midgap states, CO<sub>2</sub> photoreduction, oxygen vacancy, TiO<sub>2</sub>



## 1. INTRODUCTION

In TiO<sub>2</sub> photocatalysis, photogenerated electron–hole pairs catalyze reactions on the surface of TiO<sub>2</sub>. This property has found numerous environmentally friendly applications in various fields, such as the production of carbonaceous solar fuels, decontamination, water and air purification, and the self-cleaning surfaces.<sup>1–9</sup> Among TiO<sub>2</sub> polymorphs, anatase has been acknowledged to have superior photocatalytic properties in some previous works,<sup>10–12</sup> partially due to the larger electron effective mass of anatase, which leads to a lower mobility of charge carriers.<sup>13</sup> However, some other groups demonstrated that the catalytic activity is higher when TiO<sub>2</sub> contains a mixture of phases rather than just a single phase due to the synergistic effect of a mixed-phase as well as the robust separation of photoexcited charge carriers between several phases.<sup>14–17</sup> Nevertheless, the application of TiO<sub>2</sub> has been limited to the ultraviolet (UV) range, which makes it an inefficient photocatalyst for the solar spectrum. Narrowing down the TiO<sub>2</sub> bandgap to turn it into an efficient material for solar energy conversion has been an ongoing challenge. Several reviews highlight the advances in the field of visible light active

TiO<sub>2</sub> photocatalysts for environmental applications.<sup>18–21</sup> The previous efforts to make use of TiO<sub>2</sub> under solar radiation have been based mainly on a doping approach to modify its electronic band structure.<sup>22–27</sup> Recently, surface phases of pure TiO<sub>2</sub> with lower bandgap have been suggested as an alternative to the doping strategy.<sup>28</sup> In bulk TiO<sub>2</sub>, the lower apparent bandgap of the surface is likely caused by surface-state-induced band bending.<sup>29</sup> These states are related to Ti interstitial species that diffuse to the surface in the presence of oxygen to form a new TiO<sub>2</sub> phase,<sup>30</sup> or oxygen vacancies.<sup>31</sup> However, these phases can only form under vacuum and at elevated temperatures.<sup>28,30</sup>

The key aspects of surface and crystal facet engineering of transition metal oxide photocatalysts have been summarized in several recent reviews.<sup>28,32</sup> The previous efforts mainly investigated the contribution of surface and subsurface defects in the bulk TiO<sub>2</sub> to the bandgap states.<sup>31,33,34</sup> The focus of this

Received: October 7, 2014

Revised: November 27, 2014

Published: December 1, 2014



study is a quantitative evaluation of the electronic band structure of surfactant-free undoped mixed-phase  $\text{TiO}_2$  nanoparticles with a reduced midgap-states-induced energy gap. The  $\text{TiO}_2$  nanoparticles were obtained via a facile solution-phase method at a low temperature. This method of synthesis enables the tailoring of  $\text{TiO}_2$  physicochemical properties.<sup>35</sup> In the current study, a quantitative analysis of the bandgap states of  $\text{TiO}_2$  nanoparticles in combination with visible light-induced gas phase photoreduction of  $\text{CO}_2$  confirmed the significant role of the midgap states in lowering the energy gap and the catalytic response to the solar and the visible light.

## 2. EXPERIMENTAL SECTION

**2.1. Synthesis.** Titanium(IV) isopropoxide (TTIP, 99.999% trace metals basis) and hydrogen peroxide ( $\text{H}_2\text{O}_2$ , 30%) were purchased from Sigma-Aldrich and J.T. Baker, respectively. The peroxotitanium complex (i.e., the  $\text{TiO}_2$  amorphous solution) was prepared as explained in our earlier work.<sup>35</sup> Initially, 3.75 mL of TTIP was added dropwise to a 30 mL stirring solution of  $\text{H}_2\text{O}_2$  at room temperature. Then deionized (DI) water was added to a final volume of 100 mL after which the pH of the resultant solution was adjusted at 7.0 using  $\text{NH}_4\text{OH}$ . To obtain the crystalline phase, the peroxotitanium complex was refluxed for 10 h at 90 °C.<sup>12</sup>  $\text{TiO}_2$  nanoparticles were electrophoretically separated from the crystalline sol and dried at low temperature (90 °C) for 2 h in an electric furnace to evaporate the solvent and its byproducts. The remaining powders were collected for the analysis. The electrophoresis apparatus was composed of stainless steel anode and cathode electrodes. The electrodes were placed vertically in a beaker containing the crystalline  $\text{TiO}_2$  nanoparticle solution. The separation was carried out by applying 5 V across the cell, until the solvent and the  $\text{TiO}_2$  particles were completely segregated. The solvent was extracted using a syringe and the gel was collected for subsequent drying.

**2.2. Structural and Chemical Analysis.** The diffused reflectance spectrum (DRS) of the  $\text{TiO}_2$  sample was measured using a JASCO V-670 UV-vis-NIR spectrophotometer in a wavelength range of 200 to 800 nm with a scan speed of 100 nm min<sup>-1</sup>. The surface area, pore size, and pore volume of the synthesized  $\text{TiO}_2$  samples were determined by collecting the  $\text{N}_2$  sorption isotherms at 77 K using the Micromeritics Surface Area and Porosity analyzer ASAP-2020. In order to study the crystallinity and the crystal orientation of the synthesized  $\text{TiO}_2$  nanoparticles, X-ray diffraction (XRD) measurements were performed at room temperature (25 °C) using a D8 Advance Bruker AXS X-ray diffractometer with Cu  $\text{K}\alpha$  radiation (1.54060 Å),  $\text{K}\alpha_1$  (1.54060 Å),  $\text{K}\alpha_2$  (1.54443 Å), and  $\text{K}\beta$  (1.39222 Å). The voltage and current of the X-ray generator were adjusted at 40 kV and 40 mA, respectively. Further multielemental analyses for detection of minor and trace elements in the synthesized catalyst were performed using a quadrupole inductively coupled plasma mass spectrometry (ICP-MS, PerkinElmer ELAN DRC II). The argon gas utilized was of spectral purity (99.9998%). An aqueous multielement standard solution was used before any experiment, for consistent sensitivity. The morphology of the samples was observed using a high-resolution transmission electron microscope (HR-TEM, Tecnai F30, FEI Company) operating at 300 kV.

**2.3. Electronic Band Structure Analysis.** Au thin-film substrates (100 nm) on glass slides were purchased from EMF Corp. (Ithaca, NY). After cutting the substrates into 1 cm × 1

cm pieces, they were mounted on sample holders with two mounting screws, providing electrical contact between the Au surface and the sample holder. Before the nanoparticle deposition process, the substrates were sputter cleaned with  $\text{Ar}^+$  ions (SPECS IQE 11/35 ion source) at 5 keV for about 40 min. The samples were then transferred to the deposition chamber. The solutions containing the target materials were injected into the deposition chamber through an orifice at rates of 4 mL/h using electrospray.<sup>36</sup> A high voltage (~2000 V) was applied between the syringe needle tip and the entrance orifice assembly. A commercial multichamber system, SPECS GmbH (Berlin, Germany), with  $2 \times 10^{-10}$  mbar base pressure was used to perform inverse photoemission spectroscopy (IPES) and PES measurements. The IPES setup consists of a Kimball ELG-2/EGPS-1022 electron gun set to low energy mode, a Keithley 6485 Picoammeter to record the electron current at the substrate, and a Geiger counter to quantify the emitted photons. The Geiger-counter-based photon detector was operated in proportional mode. A  $\text{CaF}_2$  window was used as a low-pass filter with a 10.08 eV cutoff energy. Acetone vapor mixed with argon was used as the ionization gas with a 9.69 eV high-pass cutoff energy. This yielded a band-pass center-energy of 9.9 eV at an energy resolution of about 0.4 eV. The PES measurements were carried out with low-intensity X-ray photoelectron spectroscopy (LIXPS) ( $\text{Mg K}\alpha$ , 1253.6 eV, 0.1 mA emission current), UPS (He I, 21.2182 eV) and XPS ( $\text{Mg K}\alpha$ , 1253.6 eV, 20 mA emission current) in sequence.

**2.4. Activity of  $\text{CO}_2$  Photoreduction.** For each  $\text{CO}_2$  photoreduction test, 100 mg of the photocatalyst without any cocatalyst was homogeneously spread on a ~6.45 cm<sup>2</sup> base area of a stainless steel photoreactor with a quartz window. The photocatalytic tests were performed both with a commercial solar simulator (RST300S, Radiant Source Technology) at an incident light intensity of 80 mW cm<sup>-2</sup> (AM 1.0, which represents the sun spectrum after traveling through the atmosphere to the sea level with the sun directly overhead) and a visible light source (using an Edmund Optics high performance long-pass filter with the transmission wavelength of 408 to 1650 nm which avoids any interference from UV light). Both the solar and the visible light sources use a XL3000 PerkinElmer Fiber Optic Illumination (FOI) system that employs a 300-W Cermax Xenon light source (see the Supporting Information (SI) Figure S1 for the typical AM 1.0 solar spectral irradiance). The experiments were performed in a closed chamber to avoid interference with ambient lights. The reactor volume was ~10 mL. The photoreactor was vacuum-treated several times after which the high purity  $\text{CO}_2$  gas (99.99%, Airgas Inc.) was continuously passed through a water bubbler to create a mixture of  $\text{CO}_2$  saturated with  $\text{H}_2\text{O}$  vapor. Then, the mixture was flowed through the reactor system for a period of 30 min to reach equilibrium with the catalyst prior to closing the inlet and outlet valves. The reactor was operated in batch mode at a pressure of 20 psi and an isothermal temperature of 40 °C. During the illumination, samples of gas (each 80  $\mu\text{L}$ ) were taken from the reaction cell by a gastight syringe (Hamilton, 100  $\mu\text{L}$ ) and were manually injected to a gas chromatograph (GC, Agilent 6890N) equipped with a thermal conductivity detector (TCD) for subsequent concentration analysis. To evaluate the stability of the catalyst (which also might imply the stability of the midgap states), the same batch of catalyst used above, was tested again under visible light illumination in a similar photocatalytic experiment after 106 days.

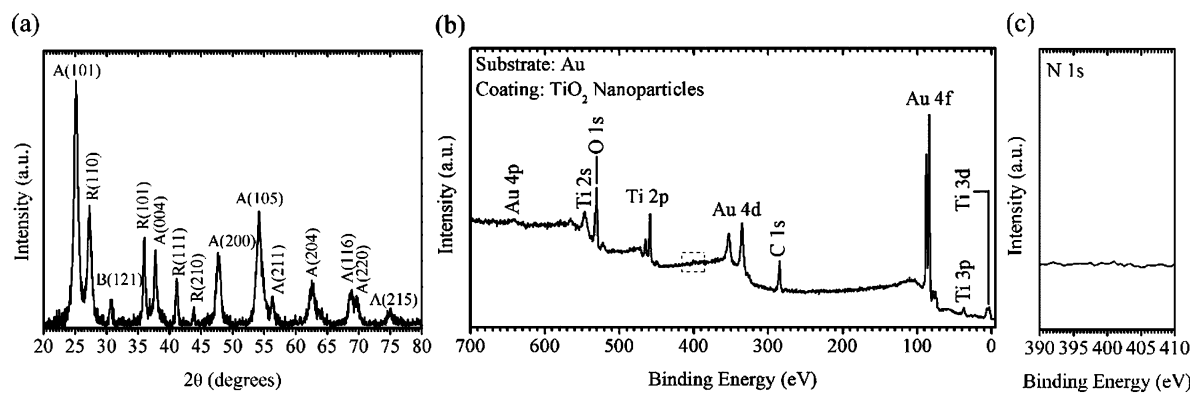


**Figure 1.** (a) X-ray diffraction (XRD) profiles of the synthesized  $\text{TiO}_2$  nanopowders (A: anatase, R: rutile, and B: brookite). (b) XPS survey spectrum of  $\text{TiO}_2$  nanoparticle thin film. (c) Close-up view of the dashed rectangle in part a, showing absence of any nitrogen-containing groups in the  $\text{TiO}_2$ .

### 3. RESULTS AND DISCUSSION

**3.1. Crystal Structure and Composition of  $\text{TiO}_2$  Polymorphs.** Figure 1 shows the X-ray diffraction (XRD) pattern of the synthesized  $\text{TiO}_2$  nanoparticles. The described preparation method led to formation of a complex crystalline mixture comprising anatase, rutile, and brookite. The main anatase  $\text{TiO}_2$  diffraction lines of (101), (004), (200), (105), and (204) were observed at  $2\theta = 25.06^\circ, 37.76^\circ, 47.97^\circ, 54.19^\circ$ , and  $62.87^\circ$ , respectively. The  $\text{TiO}_2$  diffraction lines of (110), (101), (111), and (210) at  $2\theta = 27.25^\circ, 35.97^\circ, 41.14^\circ$ , and  $43.86^\circ$ , respectively, can be indexed to the rutile polymorph. The peak at  $2\theta = 30.60^\circ$  can be assigned to (121) crystal plane of brookite  $\text{TiO}_2$  (see SI Table S1 which shows a summary of the XRD data). Annealing  $\text{TiO}_2$  nanopowders at higher temperatures ( $200^\circ\text{C}$ ) had only minor effects on the crystalline properties of the three polymorphs (see SI Figure S2 for further details). The average crystallite size of the anatase, rutile, and brookite phases were calculated at 13.4, 14.7, and 17.8 nm, respectively, using the Scherrer equation from the full-width at half-maximum (fwhm) of the most intense diffraction peaks (i.e., (101), (110), and (121)).<sup>6,35</sup>

X-ray photoelectron spectroscopy (XPS) has been employed as a sensitive technique for nitrogen (N) detection by various research groups.<sup>25–27,37–40</sup> Irie et al. have demonstrated that for a doped  $\text{TiO}_2$  structure with nitrogen ( $\text{TiO}_{2-x}\text{N}_x$ ) with  $x$  as low as 0.011, XPS can detect the N 1s core electrons.<sup>38</sup> The XPS survey spectrum and the N 1s core emission study of the  $\text{TiO}_2$  nanoparticle thin film in this work did not show any evidence of the presence of any nitrogen (Figure 1b,c).

There is always a minor amount of C 1s emission (carbon contamination) which may result from either the ex situ preparation process or the transfer process of the sample into the vacuum chamber, as it has been shown in other works.<sup>36,39</sup>

Liu et al. explained that the contamination carbon is not incorporated into the  $\text{TiO}_2$  film and it only occurs on the surface of the film as the intensity of C 1s signal can significantly be decreased with Ar ion sputtering.<sup>39</sup> As it is shown later in “Activity of  $\text{CO}_2$  Photoreduction” (section 3.6), background tests proved that the contamination carbon does not contribute in creation of carbon-containing products. Additionally, further multielemental analyses using ICP-MS with a part-per-billion (ppb) detection resolution, showed only a presence of 2.7 and 3.4 ppm of Ca and Cu, respectively, which evidence the production of an ultrapure catalyst. Hence,

these observations demonstrate that the  $\text{TiO}_2$  nanostructure is indeed undoped.

**3.2. Size and Morphology of  $\text{TiO}_2$  Polymorphs.** The morphology of the synthesized  $\text{TiO}_2$  nanoparticles was observed using a HR-TEM machine. As Figure 2a demonstrates

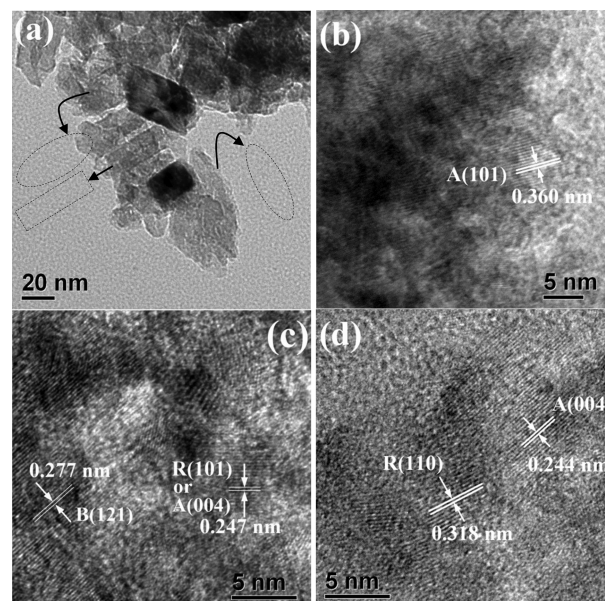


**Figure 2.** (a) TEM photograph of the synthesized  $\text{TiO}_2$  nanopowders showing agglomerates of nanosize particles. (b) HR-TEM lattice image of A(101). (c) HR-TEM lattice image of B(121), and A(004) or R(101). (d) HR-TEM lattice image of R(110) and A(004). HR-TEM images were labeled with examples of A: anatase, R: rutile, and B: brookite.

the  $\text{TiO}_2$  sample mostly consists of irregularly shaped nanoparticles, while some nanoflakes can be observed on the edges of the aggregate structure. Figure 2b shows crystals with interplanar spacing of 0.360 nm that matches the lattice spacing of (101) atomic plane of anatase  $\text{TiO}_2$ .<sup>41,42</sup> In excellent agreement with this observation, the XRD profile recorded in Figure 1 demonstrates that the interplanar distance of the (101) diffraction peak (i.e., the most intense reflection among different polymorphs) is  $d_{101} = 0.355\text{ nm}$  (SI Table S1). It has been shown previously that the lattice fringes of anatase (101) atomic plane can vary from 0.349 to 0.360 nm.<sup>8,41,43,44</sup>

Additionally, the interplanar spacing of 0.277 nm in Figure 2c is likely associated with the distance between the (121) crystal plane of the brookite phase.

The high-resolution TEM image (Figure 2c) also shows a 0.247 nm distance of the visible lattice fringes, which can be related to the lattice spacing of anatase (004) or rutile (101) atomic planes. The lattice fringes in Figure 2d suggest two interplanar distances of ~0.318 nm and ~0.244 nm, corresponding to rutile (110) and anatase (004), respectively.<sup>3,43</sup> These results are in agreement with the XRD pattern analysis. Additionally, other families of facets were recognized (SI, Figure S3), for example, rutile (101), rutile (111), and anatase (010)-type facets.

### 3.3. Surface Area and Porosity of the Synthesized TiO<sub>2</sub> Nanoparticles.

Figure 3a demonstrates the sorption

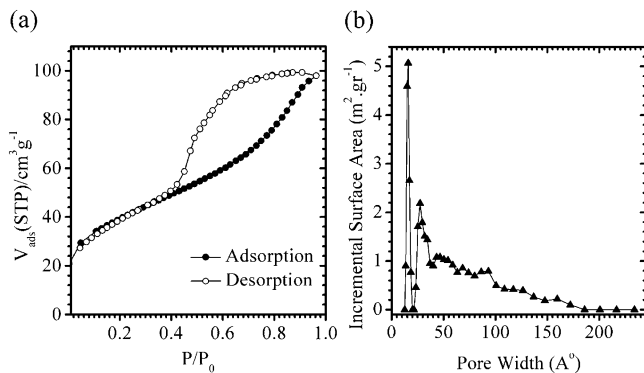


**Figure 3.** (a) Adsorption (black circles) and desorption (open circles) isotherms of N<sub>2</sub> on the synthesized TiO<sub>2</sub> nanoparticles. (b) Pore size distributions of the synthesized TiO<sub>2</sub> nanoparticles.

isotherms of N<sub>2</sub> on the synthesized TiO<sub>2</sub> sample. The plot in Figure 3a shows the typical type-IV isotherm which occurs on mesoporous adsorbents. The Langmuir and Brunauer–Emmett–Teller (BET) specific surface areas were calculated at 165.83 m<sup>2</sup> gr<sup>-1</sup> and 131.23 m<sup>2</sup> gr<sup>-1</sup>, respectively. As surface area plays a significant role in the photocatalytic reactions due to the adsorption of the reactant and the more active sites for the photoreaction,<sup>45,46</sup> the relatively large surface area of the synthesized nanoparticles can be favorable for an improved photocatalytic activity.

The pore size distribution analysis in Figure 3b indicated that the pore size of the TiO<sub>2</sub> nanoparticles falls in the range of 12.69 Å to 233.93 Å with a total volume of 0.10842 cm<sup>3</sup> gr<sup>-1</sup>. Table 1 represents the measured surface areas, pore size, and pore volume of the TiO<sub>2</sub> sample.

**3.4. Optical Bandgap and Sub-Bandgap Absorption Analysis.** The optical absorption of the TiO<sub>2</sub> sample is shown in Figure 4. The absorption is represented by the transformed Kubelka–Munk spectrum calculated from the DRS, which usually applies to highly scattering materials. High light absorption by scattering is an important factor that determines the photocatalytic activity of the TiO<sub>2</sub>. The optical absorption coefficient ( $\alpha$ ) is calculated using reflectance data according to the Kubelka–Munk equation,<sup>47</sup>  $F(R) = \alpha = (1 - R)^2 / 2R$ ,

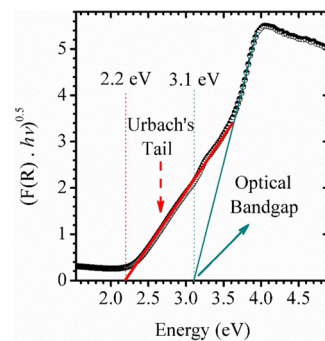


**Figure 4.** Plot of transformed Kubelka–Munk function vs the energy of the excitation source absorbed. The optical bandgap (narrow green line) and the Urbach tail (bold red line) are shown.

where  $R$  is the percentage of reflected light. The incident photon energy ( $h\nu$ ) and the optical bandgap energy ( $E_g$ ) are related to the transformed Kubelka–Munk function,  $[F(R) \cdot h\nu]^{0.5} = A(h\nu - E_g)$ , where  $E_g$  is the bandgap energy and  $A$  is the constant depending on transition probability.

From the DRS spectrum, optical bandgap—i.e., the threshold for photons to be absorbed—of the TiO<sub>2</sub> sample is determined to be ~3.1 eV from the extrapolation of the linear part of  $[F(R) \cdot h\nu]^{0.5}$  plot, based on the indirect transition. Interestingly, it is clear that a large Urbach tail is presented in the absorption spectrum which gives a significantly lower energy gap of ~2.2 eV. In TiO<sub>2</sub> photocatalysis, the photoinduced electron hole pairs catalyze the reactions on the surface of TiO<sub>2</sub> and lead to its photocatalytic activity.<sup>48</sup> These photoinduced free electrons and holes are generated by absorbing photons with energy matching or exceeding the bandgap of the TiO<sub>2</sub> nanoparticles. In our case, the tail absorption (evidenced by DRS) can contribute significantly to the absorption of photons with energies lower than the optical gap, a phenomenon known as enhanced sub-bandgap absorption.<sup>37,49</sup> The presence of this tail in the DRS spectrum may reflect the existence of disorders/defects which leads to the formation of localized states extended in the bandgap (known as midgap states).<sup>50,51</sup> The subsequent UPS and XPS studies later in this work provide further evidence on the existence of the midgap states and their origin. Additionally, the effect of the midgap states and the enhanced sub-bandgap absorption on the TiO<sub>2</sub> photocatalytic activity is studied later by the photo-reduction of CO<sub>2</sub> under both solar and visible light illuminations.

**3.5. Surface Physics and Electronic Band Structure Analysis.** In order to better comprehend the mechanism of the photocatalytic activity as well as the band structure, the electronic structure of the prepared TiO<sub>2</sub> nanoparticles was investigated using LIXPS, UPS, XPS, and IPES. In these experiments, a thin-film of TiO<sub>2</sub> nanoparticles was deposited on an Ar<sup>+</sup> sputter cleaned Au substrate. The secondary edge spectral cutoffs acquired via LIXPS allowed for the determination of the work function (WF) of the TiO<sub>2</sub> nanoparticles (Figure 5a). Figure 5a demonstrates the corresponding LIXPS measurements performed before and after UPS measurement.

**Table 1. BET and Langmuir Surface Areas (SA), Pore Size, and Pore Volume of the TiO<sub>2</sub> Samples**

sample	BET SA (m <sup>2</sup> /gr)	Langmuir SA (m <sup>2</sup> /gr)	pore size a (Å)	volume, pores a (cm <sup>3</sup> /gr)	pore size b (Å)	volume, pores b (cm <sup>3</sup> /gr)
TiO <sub>2</sub>	131.23	165.83	>12.7	0.01140	≤234	0.09702

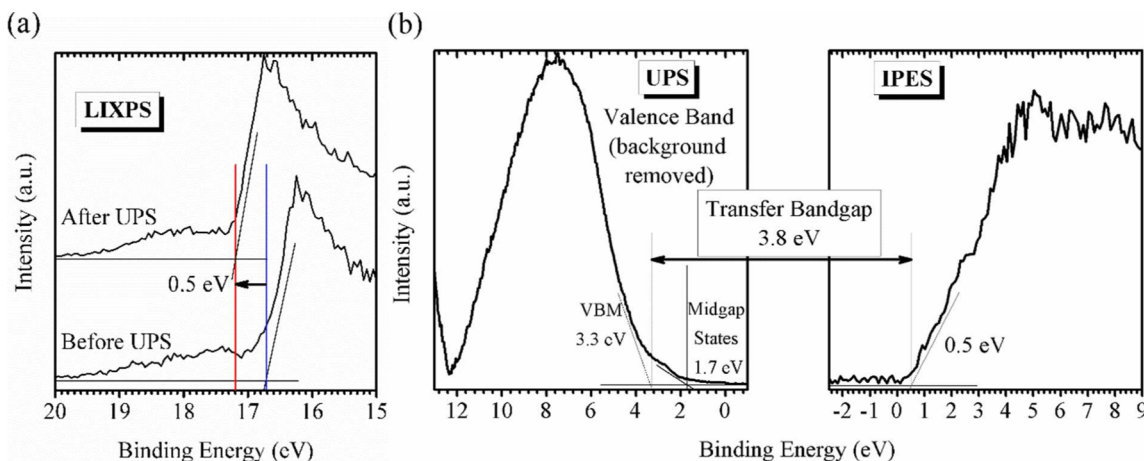


**Figure 5.** (a) Normalized secondary electron cutoff of low-intensity XP-spectra on a nanocrystalline  $\text{TiO}_2$  thin-film before and after UPS measurements. Bottom spectra allow the determination of the WF before UV exposure. The shift of the secondary edge is due to the exposure to UV light during the UPS measurements which resulted in a WF reduction. (b) The combined UPS and IPES spectra of the  $\text{TiO}_2$  nanoparticles. The left spectrum refers to the valence region measured, using UPS after background subtraction. The right spectrum represents the conduction band above the Fermi level, measured using IPES with 20 scans.

A difference between the LIXPS value before and after UPS is related to the UV-induced photochemical hydroxylation of the oxide surface.<sup>36,52</sup> As it has been demonstrated earlier, hydroxylation causes an oriented dipole on the surface with the positively charged hydrogen atom directed outward, resulting in a change in the secondary edges.<sup>52</sup> The WF was calculated by subtracting the cutoff binding energy value from the He I excitation energy (21.2182 eV) and taking the analyzer broadening of 0.1 eV into account. The WF of the  $\text{TiO}_2$  nanoparticle film was measured to be 4.5 eV (from the initial LIXPS measurement before UPS, which is free from UV-induced photochemical hydroxylation), which is in good agreement with previously reported values.<sup>36</sup> Figure 5b shows the combined UPS and IPES spectra of the synthesized  $\text{TiO}_2$  nanoparticles.

The valence band maximum (VBM) was determined to be 3.3 eV below the Fermi level. The conduction band edge (measured by IPES) was determined to be 0.5 eV above the Fermi level. Hence, the corresponding transfer bandgap (electronic bandgap) of the prepared  $\text{TiO}_2$  nanoparticles was estimated to be about 3.8 eV. As  $\text{TiO}_2$  is a semiconductor material with a large exciton binding energy, the transfer/electronic bandgap (3.8 eV) of  $\text{TiO}_2$ —i.e. the threshold for creating an unbound electron–hole pair—is at a higher energy than the optical bandgap (3.1 eV, Figure 4), which was measured earlier in this work using DRS. Additionally, the electronic bandgap of  $\text{TiO}_2$  nanoparticles are strongly dependent on the synthesis method and the particle size.<sup>36</sup>

The ultraviolet photoemission (UP)-spectrum in Figure 5b shows a clear feature with an edge of 1.7 eV. This feature is related to the midgap states of the  $\text{TiO}_2$  nanoparticles,<sup>36</sup> which was earlier presented in this work with a large Urbach tail in the DRS spectrum. Considering the UP-spectrum in Figure 5b, the edge of the  $\text{TiO}_2$  midgap states, which was measured at 1.7 eV below the Fermi level, establishes a 2.2 eV midgap-states-induced energy gap, which also explains the observed Urbach tail in the optical absorption spectrum. Therefore, these states in the  $\text{TiO}_2$  bandgap may provide the major pathway for electron transfer between the semiconductor nanoparticles and the acceptor species.<sup>53</sup> The excess electrons originating from localized states can greatly affect the surface chemistry of

$\text{TiO}_2$ .<sup>54</sup> Hence, it is reasonable to assume that the midgap states of the  $\text{TiO}_2$  nanoparticles can play a dominant role in its solar and visible-light response and its photocatalytic properties. Figure 6 illustrates the summarized electronic structure of the

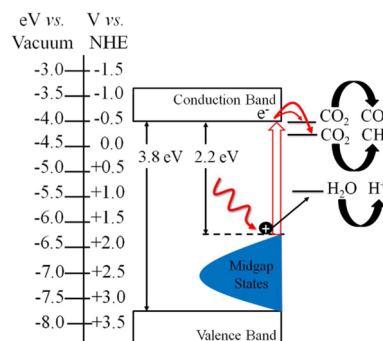


**Figure 6.** Schematic illustration of the electronic structure of the  $\text{TiO}_2$  nanoparticles combined with proposed diagram of  $\text{CO}_2$  photoreduction. Blue feature shows the presence of localized states extended in the bandgap which give rise to a surface induced energy gap of 2.2 eV. The energy level at each layer is relative to the vacuum level. The corresponding electrochemical potentials can be found from the normal hydrogen electrode (NHE) axis at the right.

synthesized  $\text{TiO}_2$  nanoparticles combined with proposed diagram of  $\text{CO}_2$  photoreduction. Under illumination with energies equal or greater than 2.2 eV, the generated electrons at the midgap states can be transferred to the conduction band of the semiconductor, leaving holes behind. These photo-generated electrons and holes can cause reduction and oxidation reactions, respectively. The electrons can eventually be transferred to the acceptor species such as  $\text{CO}_2$ . In the meantime, the possible hole reaction could be oxidation of water vapor ( $\text{H}_2\text{O}$ ) to  $\text{H}^+$  by generated holes in the midgap states. As it is shown in Figure 6, the top of the midgap states is more positive than the oxidation potential of  $\text{H}_2\text{O}$  to  $\text{O}_2$  ( $\text{O}_2/\text{H}_2\text{O}$  energy level is located at +0.82 V vs NHE at pH 7.0). Hence, it is reasonable to assume that photons from the visible light with enough energy can provide the driving energy for this reaction. As it has been explained in earlier works,<sup>55,56</sup> the hole

transport from the semiconductor (in this case from the midgap states) to the water vapor might be sluggish, which could slow down the kinetic and increase the overpotential. The intent of the current study is to photoreduce  $\text{CO}_2$  for production of hydrocarbon fuels using a novel transitional metal oxide. Hence, although water vapor oxidation can likely occur, as predicted by thermodynamics and based on the presented band diagram, the sluggish kinetic is not an issue for our anticipated application.

The localized electronic midgap states (responsible for the Urbach tail) can originate from point defects (such as oxygen vacancies), metal or nitrogen dopants, and/or lattice disorders.<sup>39,57–60</sup> The elemental analysis in the current study using XPS (Figure 1b,c) showed no evidence of the presence of any N. Further elemental analyses using both XPS and ICP-MS demonstrated that the synthesized catalyst is indeed pure as the amount of metal impurities in total was negligible ( $\sim 6$  ppm). Additionally, the high-resolution TEM image (Figure 2) showed that the interplanar distances of the visible lattice fringes are consistent with the lattice spacing of ordered anatase and rutile in previous works.<sup>41–44</sup> Hence, to further explore the mechanism and the origin underlying the observed midgap states, we carried out XPS Ti 2p and O 1s core emission study.

Figure 7 shows the corresponding XPS core level lines measured after the deposition of the  $\text{TiO}_2$  nanoparticles on the

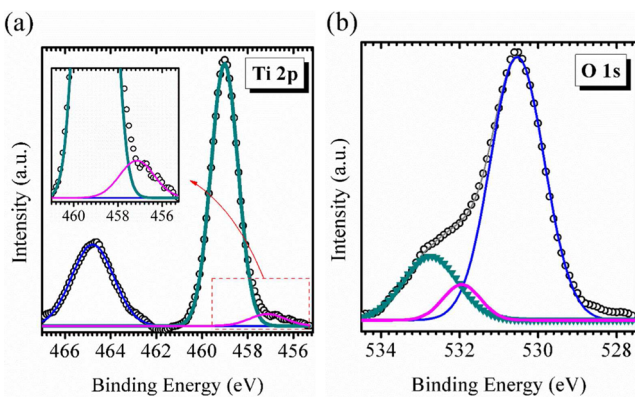


**Figure 7.** Core line emissions and defects characterization of the undoped synthesized  $\text{TiO}_2$ . (a) Ti 2p and (b) O 1s XPS core level spectra for the  $\text{TiO}_2$  nanoparticles. The core levels in both parts are shown by open circles and the corresponding fittings are shown either by solid lines or closed symbols.

Au substrate. Figure 7a,b show the  $\text{TiO}_2$ -related Ti 2p and O 1s emission lines, respectively. A detailed deconvolution analysis was performed on each spectrum to identify the contributing components.

Figure 7a clearly shows the position of the Ti 2p spin doublet with  $2p_{3/2}$  and  $2p_{1/2}$  binding energies of  $\sim 459.0$  and  $464.7$  eV, respectively. These values are in agreement with the reported figures for high-resolution Ti 2p XPS spectra of unmodified  $\text{TiO}_2$  in an earlier study.<sup>37</sup> The binding energy difference of  $5.7$  eV between the Ti 2p spin doublets indicates a valence state of +4 for Ti.<sup>61</sup> Additionally, noticeable  $\text{Ti}^{3+}$  signal was also detected with a binding energy of  $457.1$  eV (Figure 7a, inset). It has been demonstrated that the presence of small amount of  $\text{Ti}^{3+}$  in the Ti 2p spectrum could derive from an oxygen deficient surface.<sup>62</sup> Succeeding the formation of an oxygen vacancy, two  $\text{Ti}^{4+}$  cations should convert to two  $\text{Ti}^{3+}$  cations to maintain the charge neutrality. These observations are

consistent with previous studies.<sup>22,63</sup> Additionally, under illumination, the photogenerated delocalized electrons can be trapped at coordinatively unsaturated cation sites located in anatase to form  $\text{Ti}^{3+}$  species.<sup>64,65</sup> The fit of the O 1s XPS core emission profile (Figure 7b) was resolved using three different components. The major signal at  $\sim 530.5$  eV is related to the bulk Ti–O (crystal lattice oxygen).<sup>66,67</sup> The higher-energy peaks at  $532.7$  eV and  $\sim 531.9$  eV are assigned to the adsorbed surface  $\text{H}_2\text{O}$  (surface contamination layer) as well as oxygen vacancies and surface hydroxyls, respectively, as was shown in recent works.<sup>39,66,68,69</sup> Because the depth of XPS analysis is only limited to several atomic layers, these defects and adsorbed oxygen species are likely located on the surface layer of the oxide. Assigning the peak at  $531.9$  eV to oxygen vacancies together with presence of  $\text{Ti}^{3+}$  signal, is in agreement with earlier interpretations of core emission lines for identifying oxygen deficient sites.<sup>68,70,71</sup> The oxygen depletion generates excess electrons that are stabilized into the reduced solid and deeply influence its photocatalytic properties.<sup>53,54,64,72</sup> Lin et al. have shown that 3d Ti donor states that are present in the  $\text{TiO}_2$  with oxygen vacancies results in optical absorption across the visible light region.<sup>73</sup> Additionally, it has been shown in earlier studies, using density functional theory (DFT) calculations, that the presence of defects facilitates  $\text{CO}_2$  dissociation.<sup>74,75</sup> A detailed study on these defects and the behavior of the structure in terms of charge dynamics in the dark and under illumination is underway, and the results will be reported in forthcoming papers.

**3.6. Activity of  $\text{CO}_2$  Photoreduction.** The photoreduction of  $\text{CO}_2$  to carbonaceous solar fuels has drawn much attention because it helps to reduce global warming, to overcome energy shortage, and positively affects the atmospheric carbon balance.<sup>76</sup> Several reviews highlight the photo-induced activation of  $\text{CO}_2$  on Ti-based heterogeneous catalysts.<sup>77,78</sup> In this work, the heterogeneous photoelectrochemical reduction of  $\text{CO}_2$  under both the solar light and the visible light illuminations in the presence of undoped  $\text{TiO}_2$  nanoparticles were studied (Figure 8). In order to rule out possibilities of potential contamination, background tests were first conducted with a mixture of  $\text{N}_2 + \text{H}_2\text{O}$  (without introducing  $\text{CO}_2$  as the carbon source) passing through both

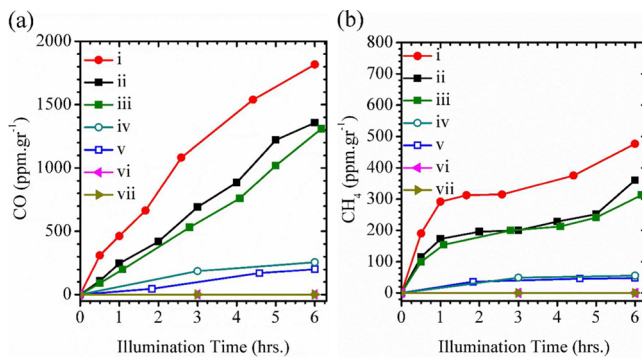


**Figure 8.** (a) CO and (b)  $\text{CH}_4$  evolutions over the prepared  $\text{TiO}_2$  and P25 standard samples (in both parts (a) and (b), i and iv: synthesized  $\text{TiO}_2$  and P25  $\text{TiO}_2$  under solar light illumination, respectively. ii and v: synthesized  $\text{TiO}_2$  and P25  $\text{TiO}_2$  under visible light illumination, respectively. iii: synthesized  $\text{TiO}_2$  under visible light illumination after 106 days (stability test). vi and vii: synthesized  $\text{TiO}_2$  and P25  $\text{TiO}_2$  with a mixture of  $\text{N}_2 + \text{H}_2\text{O}$  (without any  $\text{CO}_2$ ) under solar light illumination, respectively.

the synthesized TiO<sub>2</sub> and the standard P25 TiO<sub>2</sub> (Figure 8a,b, curves vi and vii) catalysts under photoillumination. The analysis showed that no carbon-containing product was observed. CO and CH<sub>4</sub> as photoreduction products were observed only in the presence of CO<sub>2</sub>, which supports the interpretation that CO<sub>2</sub> was indeed the carbon source. Additionally, when the photocatalysts samples in the reactor were kept in the dark (introducing CO<sub>2</sub> but without irradiation), no changes were observed in the CO<sub>2</sub> photoreduction, confirming that the photoreduction of CO<sub>2</sub> is a light-driven reaction. By measuring the concentrations of CO and CH<sub>4</sub> at the reactor outlet, the production of CO and CH<sub>4</sub>, in ppm·gr<sup>-1</sup> during a 6 h photoillumination period was calculated, and the data are shown in Figure 8. Figure 8 shows a negligible production of CH<sub>4</sub> over (P25) sample, which is in agreement with a previous report.<sup>79</sup> The overall production of CO and CH<sub>4</sub> on the synthesized TiO<sub>2</sub> nanoparticles in 6 h were measured to be ~1818 and ~477 ppm·gr<sup>-1</sup> under solar light, and ~1357 and ~360 ppm·gr<sup>-1</sup> under visible light illuminations, respectively; the photocatalytic activity of the synthesized undoped TiO<sub>2</sub> nanoparticles under visible light illumination is 6.75 and 7.66 times higher than that of TiO<sub>2</sub> (P25) standard sample in production of CO and CH<sub>4</sub>, respectively.

The photochemical quantum yields ( $\eta$  %) of CO<sub>2</sub> reduction to CO and CH<sub>4</sub> under solar irradiation (curve i, Figure 8a,b) were calculated using the following equation as explained in an earlier study.<sup>80</sup>

$$\eta_{\text{CO or CH}_4} (\%) = \frac{n \times \text{moles of reduction products (CO or CH}_4)}{\text{moles of photon absorbed by catalyst}} \times 100\% \quad (1)$$

where  $n$  is the number of electrons required to convert CO<sub>2</sub> to CO or CH<sub>4</sub>, that is two and eight, respectively. Because the surface energy gap of the synthesized TiO<sub>2</sub> was measured at 2.2 eV, photons with  $\lambda > 564$  nm would not create an unbound electron–hole. The incident light intensity of the source in the effective UV and visible range (250–564 nm) was estimated to be ~28 mW cm<sup>-2</sup> at the catalyst surface. Following the method used by Wang et al.,<sup>80</sup> the average photon energy in the range of 250 to 564 nm was estimated to be  $\sim 4.88 \times 10^{-19}$  J. The maximum CO and CH<sub>4</sub> yields for the synthesized TiO<sub>2</sub> catalysts were 0.157 and 0.041  $\mu\text{mol g}^{-1} \text{ hr}^{-1}$ , respectively (presented in ppm in Figure 8a,b, curve i). The moles of photon absorbed by catalysts (or the photon flux)—i.e., the number of photons per second per unit area—was calculated at  $57.38 \times 10^{19} \text{ m}^{-2} \cdot \text{s}^{-1}$ . Considering the base surface area of the photoreactor (6.45 cm<sup>2</sup>) and the amount of catalyst used (100 mg), the photochemical quantum yield for CO and CH<sub>4</sub> was calculated at 0.0141% and 0.0148%, respectively. The total quantum yield ( $\eta_{\text{CO}} + \eta_{\text{CH}_4}$ ) was thus obtained as 0.0289%. These results are comparable to the previously reported figures.<sup>79</sup>

To study the stability of the synthesized catalyst, the same batch of catalyst used above, was re-employed in a similar photocatalytic experiment toward photoreduction of CO<sub>2</sub> under visible light illumination, after 106 days. The obtained results (Figure 8a,b, curve iii) demonstrate that the synthesized catalyst is extremely stable because almost the same amount of CO and CH<sub>4</sub> could be obtained. This likely implies that the midgap states associated with the synthesized structure are pretty stable, as well.

Additionally, time dependence of the volumetric ratio of O<sub>2</sub>/N<sub>2</sub> during photoreduction of CO<sub>2</sub> with H<sub>2</sub>O on the synthesized

nanopowder, as an essential indicator for proton generation,<sup>80</sup> was monitored which showed an increase from ~0.26 for the air ratio to above 0.65 and 0.55 after solar and visible light irradiation, respectively. This data can be considered as a further evidence for the photocatalytic reaction of CO<sub>2</sub> with H<sub>2</sub>O in the presence of the synthesized TiO<sub>2</sub> sample, to form CO/CH<sub>4</sub> and O<sub>2</sub> (Figure 9). Time dependence of the

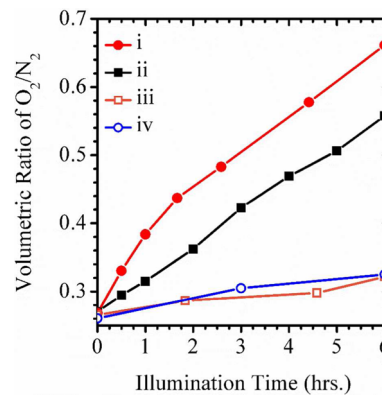


**Figure 9.** Time dependence of the volumetric ratio of O<sub>2</sub>/N<sub>2</sub> during photoreduction of CO<sub>2</sub> with H<sub>2</sub>O on the synthesized TiO<sub>2</sub> nanopowder and P25 TiO<sub>2</sub> standard sample. i and iii: synthesized TiO<sub>2</sub> and P25 TiO<sub>2</sub> under solar light illumination, respectively. ii and iv: synthesized TiO<sub>2</sub> and P25 TiO<sub>2</sub> under visible light illumination, respectively.

volumetric ratio of O<sub>2</sub>/N<sub>2</sub> toward photoreduction of CO<sub>2</sub> on the synthesized nanopowder under visible illumination after 106 days, showed similar figures to the one in Figure 9, curve ii (not shown here).

Overall, we reasoned that the photocatalytic activity of the undoped TiO<sub>2</sub> nanoparticles in the visible range can be ascribed to the unique electronic structure of their surface (due to the presence of midgap states which induce a surface energy gap of 2.2 eV) and their relatively large surface area. Under visible light illumination, the electrons could be excited from the midgap states to the conduction band. The CO<sub>2</sub> molecules can be adsorbed on a semiconductor surface and capture the transferred electrons from the defect or the trapping sites to the conduction band.<sup>78</sup>

In reality, the mechanism of CO<sub>2</sub> photoreduction is very complicated and requires determination of surface state energy levels for the CO<sub>2</sub>(gas)/CO<sub>2</sub><sup>•-</sup>(surface) couples at the TiO<sub>2</sub> surface (solid–gas interface). A former review has applied an approach comparable to that by Koppenol et al.,<sup>81</sup> and has estimated this energy level based on the adiabatic electron affinity of gaseous CO<sub>2</sub>, the heat of chemisorption of CO<sub>2</sub><sup>•-</sup> on the surface, and the overall free energy change of the reaction.<sup>78</sup> However, because the former estimation is not accurate and ignores different influential parameters such as the electrostatic contributions, the standard electrochemical potentials of the redox couples are commonly being used.<sup>77,80,82–84</sup> Additionally, it has been suggested that the mechanism of CO<sub>2</sub> photoreduction in the presence of dissociated hydrogen atoms is based on proton assisted multielectron transfer rather than a single electron transfer process, because the -1.90 V (vs NHE) standard electrochemical potential of the CO<sub>2</sub>/CO<sub>2</sub><sup>•-</sup> redox couple is highly unfavorable.<sup>79,80,85</sup> Hence, other reactions such as CO formation ( $E^\circ_{\text{redox}} = -0.52$  V vs NHE) or CH<sub>4</sub> formation ( $E^\circ_{\text{redox}} = -0.24$  V vs NHE) are energetically more

favorable to occur. In the CO<sub>2</sub> photoreduction process under illumination, CO<sub>2</sub> may interact with residing electrons at TiO<sub>2</sub> surface sites (e.g., Ti<sup>3+</sup>) and reduces into CH<sub>4</sub> via the reaction of CO<sub>2</sub> + 8H<sup>+</sup> + 8e<sup>-</sup> → CH<sub>4</sub> + 2H<sub>2</sub>O,<sup>82</sup> while the photogenerated holes in the valence band oxidize H<sub>2</sub>O into oxygen and H<sup>+</sup> via the half-reaction H<sub>2</sub>O → 1/2O<sub>2</sub> + 2H<sup>+</sup> + 2e<sup>-</sup> (Figure 6).<sup>82</sup> Water can also act as a proton donor.<sup>79</sup> To elucidate the multiple roles of water in the overall photocatalytic reduction of CO<sub>2</sub> to hydrocarbon fuels over TiO<sub>2</sub>, a mechanistic study using electron paramagnetic resonance technique is necessary which is outside the scope of the current work.

Because our controlled experiments demonstrated no evidence of CH<sub>4</sub> formation in the dark or under illumination in the absence of any catalyst, it is reasonable to conclude that CO<sub>2</sub> reduction is a light-driven catalytic reaction that occurs over the photocatalyst. Several facts may explain the lower production of CH<sub>4</sub> comparing to CO in our study including the following: multielectron transfer pathway of CH<sub>4</sub> formation, potential decomposition of CH<sub>4</sub> to CO in a reaction with photogenerated OH radicals,<sup>8</sup> and higher number of electrons and protons required for its formation. A thorough mechanistic study to probe the reaction pathways is underway in our laboratory and will be reported in forthcoming papers.

## CONCLUSIONS

In conclusion, the presented results suggest that the photocatalytic activity of the synthesized undoped mixed-phase TiO<sub>2</sub> nanoparticles is in the visible range. This can be associated with the unique electronic structure of the nanoparticles, which were studied using LIXPS, UPS, and IPES measurements. The high density of midgap states gives rise to an effective energy gap of 2.2 eV, which is responsible for the determined absorption in the visible range and the observed catalytic properties in gas phase toward photoreduction of CO<sub>2</sub>.

## ASSOCIATED CONTENT

### Supporting Information

The following file is available free of charge on the ACS Publications website at DOI: 10.1021/cs501539q.

Additional information including the typical air mass (AM) 1.0 solar spectral irradiance, 2θs, d-spacing, and relative intensity (%) of each diffraction peak of the as-prepared TiO<sub>2</sub> nanopowders, XRD profiles of the synthesized TiO<sub>2</sub> nanopowders before and after heat treatment at a moderate temperature (200 °C), and high-magnification TEM images of nanoparticles showing lattice images of R(101), R(111), A(010), and A(010) ([PDF](#))

## AUTHOR INFORMATION

### Corresponding Author

\*E-mail: hyaghoubi@mail.usf.edu. Tel.: +1-813-409-8192.

### Notes

The authors declare no competing financial interest.

## ACKNOWLEDGMENTS

The authors would like to thank Dr. Zachary Atlas and the Center for Geochemical Analysis at the University of South Florida for valuable help performing the ICP-MS analyses. This work was supported in part by the National Science Foundation through NSF DMR-0906922 and DMR 1035196.

Houman Yaghoubi would like to acknowledge the University of South Florida for partially supporting this work through an Interdisciplinary Research Grant.

## REFERENCES

- Fujishima, A.; Zhang, X.; Tryk, D. A. *Surf. Sci. Rep.* **2008**, *63*, S15–S82.
- Fujishima, A.; Zhang, X. *C. R. Chim.* **2006**, *9*, 750–760.
- Fujishima, A.; Nakata, K.; Ochiai, T.; Manivannan, A.; Tryk, D. A. *Electrochim. Soc. Interface* **2013**, *22*, S1–S6.
- Ganesh, V. A.; Raut, H. K.; Nair, A. S.; Ramakrishna, S. *J. Mater. Chem.* **2011**, *21*, 16304–16322.
- Wu, D.; Long, M. *ACS Appl. Mater. Interfaces* **2011**, *3*, 4770–4774.
- Yaghoubi, H.; Taghavinia, N.; Alamdar, E. K.; Volinsky, A. A. *ACS Appl. Mater. Interfaces* **2010**, *2*, 2629–2636.
- Ismail, A. A.; Bahnemann, D. W. *J. Mater. Chem.* **2011**, *21*, 11686–11707.
- Liu, L.; Zhao, H.; Andino, J. M.; Li, Y. *ACS Catal.* **2012**, *2*, 1817–1828.
- Yaghoubi, H. *Self-Cleaning Materials and Surfaces*; John Wiley & Sons, Ltd: Chichester, U.K., 2013; pp 153–202.
- Fox, M. A.; Dulay, M. T. *Chem. Rev.* **1993**, *93*, 341–357.
- Kubacka, A.; Fernández-García, M.; Colón, G. *Chem. Rev.* **2011**, *112*, 1555–1614.
- Yaghoubi, H.; Taghavinia, N.; Alamdar, E. K. *Surf. Coat. Technol.* **2010**, *204*, 1562–1568.
- Mo, S.-D.; Ching, W. Y. *Phys. Rev. B: Condens. Matter Mater. Phys.* **1995**, *51*, 13023–13032.
- Nonoyama, T.; Kinoshita, T.; Higuchi, M.; Nagata, K.; Tanaka, M.; Sato, K.; Kato, K. *J. Am. Chem. Soc.* **2012**, *134*, 8841–8847.
- Kho, Y. K.; Iwase, A.; Teoh, W. Y.; Mädler, L.; Kudo, A.; Amal, R. *J. Phys. Chem. C* **2010**, *114*, 2821–2829.
- Zachariah, A.; Baiju, K. V.; Shukla, S.; Deepa, K. S.; James, J.; Warrier, K. G. K. *J. Phys. Chem. C* **2008**, *112*, 11345–11356.
- Scanlon, D. O.; Dunnill, C. W.; Buckeridge, J.; Shevlin, S. A.; Logsdail, A. J.; Woodley, S. M.; Catlow, C. R. A.; Powell, M. J.; Palgrave, R. G.; Parkin, I. P.; Watson, G. W.; Keal, T. W.; Sherwood, P.; Walsh, A.; Sokol, A. A. *Nat. Mater.* **2013**, *12*, 798–801.
- Pelaez, M.; Nolan, N. T.; Pillai, S. C.; Seery, M. K.; Falaras, P.; Kontos, A. G.; Dunlop, P. S. M.; Hamilton, J. W. J.; Byrne, J. A.; O’Shea, K.; Entezari, M. H.; Dionysiou, D. D. *Appl. Catal., B* **2012**, *125*, 331–349.
- Kumar, S. G.; Devi, L. G. *J. Phys. Chem. A* **2011**, *115*, 13211–13241.
- Daghrir, R.; Drogui, P.; Robert, D. *Ind. Eng. Chem. Res.* **2013**, *52*, 3581–3599.
- Ni, M.; Leung, M. K. H.; Leung, D. Y. C.; Sumathy, K. *Renewable Sustainable Energy Rev.* **2007**, *11*, 401–425.
- Liu, G.; Yin, L.-C.; Wang, J.; Niu, P.; Zhen, C.; Xie, Y.; Cheng, H.-M. *Energy Environ. Sci.* **2012**, *5*, 9603–9610.
- Yu, J. C.; Yu, J.; Ho, W.; Jiang, Z.; Zhang, L. *Chem. Mater.* **2002**, *14*, 3808–3816.
- Park, J. H.; Kim, S.; Bard, A. J. *Nano Lett.* **2005**, *6*, 24–28.
- Burda, C.; Lou, Y.; Chen, X.; Samia, A. C. S.; Stout, J.; Gole, J. L. *Nano Lett.* **2003**, *3*, 1049–1051.
- Diwald, O.; Thompson, T. L.; Zubkov, T.; Walck, S. D.; Yates, J. T. *J. Phys. Chem. B* **2004**, *108*, 6004–6008.
- Asahi, R.; Morikawa, T.; Ohwaki, T.; Aoki, K.; Taga, Y. *Science* **2001**, *293*, 269–271.
- Batzill, M. *Energy Environ. Sci.* **2011**, *4*, 3275–3286.
- Zhang, Z.; Yates, J. T. *Chem. Rev.* **2012**, *112*, 5520–5551.
- Tao, J.; Luttrell, T.; Batzill, M. *Nat. Chem.* **2011**, *3*, 296–300.
- Mao, X.; Lang, X.; Wang, Z.; Hao, Q.; Wen, B.; Ren, Z.; Dai, D.; Zhou, C.; Liu, L.-M.; Yang, X. *J. Phys. Chem. Lett.* **2013**, *4*, 3839–3844.
- Liu, G.; Yu, J. C.; Lu, G. Q.; Cheng, H.-M. *Chem. Commun.* **2011**, *47*, 6763–6783.

- (33) Yim, C. M.; Pang, C. L.; Thornton, G. *Phys. Rev. Lett.* **2010**, *104*, 036806(1–4).
- (34) Krüger, P.; Jupille, J.; Bourgeois, S.; Domenichini, B.; Verdini, A.; Floreano, L.; Morgante, A. *Phys. Rev. Lett.* **2012**, *108*, 126803(1–4).
- (35) Yaghoubi, H.; Dayerizadeh, A.; Han, S.; Mulaj, M.; Gao, W.; Li, X.; Muschol, M.; Ma, S.; Takshi, A. *J. Phys. D: Appl. Phys.* **2013**, *46*, 505316(1–10).
- (36) Li, Z.; Berger, H.; Okamoto, K.; Zhang, Q.; Luscombe, C. K.; Cao, G.; Schlaf, R. *J. Phys. Chem. C* **2013**, *117*, 13961–13970.
- (37) Beranek, R.; Kisch, H. *Photochem. Photobiol. Sci.* **2008**, *7*, 40–48.
- (38) Irie, H.; Watanabe, Y.; Hashimoto, K. *J. Phys. Chem. B* **2003**, *107*, 5483–5486.
- (39) Liu, G.; Jaegermann, W.; He, J.; Sundström, V.; Sun, L. *J. Phys. Chem. B* **2002**, *106*, 5814–5819.
- (40) Ananpattarachai, J.; Kajitvichyanukul, P.; Seraphin, S. *J. Hazard. Mater.* **2009**, *168*, 253–261.
- (41) Liu, S. M.; Gan, L. M.; Liu, L. H.; Zhang, W. D.; Zeng, H. C. *Chem. Mater.* **2002**, *14*, 1391–1397.
- (42) Jiang, Y.-M.; Wang, K.-X.; Zhang, H.-J.; Wang, J.-F.; Chen, J.-S. *Sci. Rep.* **2013**, *3*, 1–5.
- (43) Liu, B.; Khare, A.; Aydil, E. S. *Chem. Commun.* **2012**, *48*, 8565–8567.
- (44) Dai, S.; Wu, Y.; Sakai, T.; Du, Z.; Sakai, H.; Abe, M. *Nanoscale Res. Lett.* **2010**, *5*, 1829–1835.
- (45) Xu, H.; Ouyang, S.; Li, P.; Kako, T.; Ye, J. *ACS Appl. Mater. Interfaces* **2013**, *5*, 1348–1354.
- (46) Chen, X.; Li, Z.; Ye, J.; Zou, Z. *Chem. Mater.* **2010**, *22*, 3583–3585.
- (47) Lin, H.; Huang, C. P.; Li, W.; Ni, C.; Shah, S. I.; Tseng, Y.-H. *Appl. Catal., B* **2006**, *68*, 1–11.
- (48) Houas, A.; Lachheb, H.; Ksibi, M.; Elaloui, E.; Guillard, C.; Herrmann, J.-M. *Appl. Catal., B* **2001**, *31*, 145–157.
- (49) John, S.; Soukoulis, C.; Cohen, M. H.; Economou, E. N. *Phys. Rev. Lett.* **1986**, *57*, 1777–1780.
- (50) Könenkamp, R. *Phys. Rev. B: Condens. Matter Mater. Phys.* **2000**, *61*, 11057–11064.
- (51) Nagpal, P. K.; Victor, I. *Nat. Commun.* **2011**, *2*:486, 1–7.
- (52) Gutmann, S.; Wolak, M. A.; Conrad, M.; Beerbom, M. M.; Schlaf, R. *J. Appl. Phys.* **2011**, *109*, 113719(1–10).
- (53) Mora-Seró, I.; Bisquert, J. *Nano Lett.* **2003**, *3*, 945–949.
- (54) Deskins, N. A.; Rousseau, R.; Dupuis, M. *J. Phys. Chem. C* **2010**, *114*, 5891–5897.
- (55) Maeda, K. *ACS Catal.* **2013**, *3*, 1486–1503.
- (56) Bassi, P. S.; Gurudyal; Wong, L. H.; Barber, J. *Phys. Chem. Chem. Phys.* **2014**, *16*, 11834–11842.
- (57) Chen, X.; Liu, L.; Yu, P. Y.; Mao, S. S. *Science* **2011**, *331*, 746–750.
- (58) Umebayashi, T.; Yamaki, T.; Itoh, H.; Asai, K. *J. Phys. Chem. Solids* **2002**, *63*, 1909–1920.
- (59) Choi, J.; Park, H.; Hoffmann, M. R. *J. Phys. Chem. C* **2009**, *114*, 783–792.
- (60) Nakamura, R.; Tanaka, T.; Nakato, Y. *J. Phys. Chem. B* **2004**, *108*, 10617–10620.
- (61) Chandana, R.; Mohanty, P.; Pandey, A. C.; Mishra, N. C. *J. Phys. D: Appl. Phys.* **2009**, *42*, 205101(1–6).
- (62) Pan, J. M.; Maschhoff, B. L.; Diebold, U.; Madey, T. E. *J. Vac. Sci. Technol., A* **1992**, *10*, 2470–2476.
- (63) Diebold, U. *Surf. Sci. Rep.* **2003**, *48*, 53–229.
- (64) Chiesa, M.; Paganini, M. C.; Livraghi, S.; Giannello, E. *Phys. Chem. Chem. Phys.* **2013**, *15*, 9435–9447.
- (65) Livraghi, S.; Chiesa, M.; Paganini, M. C.; Giannello, E. *J. Phys. Chem. C* **2011**, *115*, 25413–25421.
- (66) Hu, W.; Liu, Y.; Withers, R. L.; Frankcombe, T. J.; Norén, L.; Snashall, A.; Kitchin, M.; Smith, P.; Gong, B.; Chen, H.; Schiemer, J.; Brink, F.; Wong-Leung, J. *Nat. Mater.* **2013**, *12*, 821–826.
- (67) Jing, L.; Xin, B.; Yuan, F.; Xue, L.; Wang, B.; Fu, H. *J. Phys. Chem. B* **2006**, *110*, 17860–17865.
- (68) Ramos-Moore, E.; Ferrari, P.; Diaz-Droguett, D. E.; Lederman, D.; Evans, J. T. *J. Appl. Phys.* **2012**, *111*, 014108(1–8).
- (69) Carreras, P.; Gutmann, S.; Antony, A.; Bertomeu, J.; Schlaf, R. *J. Appl. Phys.* **2011**, *110*, 073711(1–7).
- (70) Zou, Q.; Ruda, H.; Yacobi, B. G.; Farrell, M. *Thin Solid Films* **2002**, *402*, 65–70.
- (71) Kuznetsov, M. V.; Zhuravlev, J. F.; Gubanov, V. A. *J. Electron Spectrosc. Relat. Phenom.* **1992**, *58*, 169–176.
- (72) Nakamura, I.; Negishi, N.; Kutsuma, S.; Ihara, T.; Sugihara, S.; Takeuchi, K. *J. Mol. Catal. A: Chem.* **2000**, *161*, 205–212.
- (73) Lin, Z.; Orlov, A.; Lambert, R. M.; Payne, M. C. *J. Phys. Chem. B* **2005**, *109*, 20948–20952.
- (74) Yang, C.-T.; Balakrishnan, N.; Bhethanabotla, V. R.; Joseph, B. *J. Phys. Chem. C* **2014**, *118*, 4702–4714.
- (75) Yang, C.-T.; Wood, B. C.; Bhethanabotla, V. R.; Joseph, B. *J. Phys. Chem. C* **2014**, *118*, 26236–26248.
- (76) Cheng, H.; Huang, B.; Liu, Y.; Wang, Z.; Qin, X.; Zhang, X.; Dai, Y. *Chem. Commun.* **2012**, *48*, 9729–9731.
- (77) Dhakshinamoorthy, A.; Navalon, S.; Corma, A.; Garcia, H. *Energy Environ. Sci.* **2012**, *5*, 9217.
- (78) Indrakanti, V. P.; Kubicki, J. D.; Schobert, H. H. *Energy Environ. Sci.* **2009**, *2*, 745–758.
- (79) Dimitrijevic, N. M.; Vijayan, B. K.; Poluektov, O. G.; Rajh, T.; Gray, K. A.; He, H.; Zapol, P. *J. Am. Chem. Soc.* **2011**, *133*, 3964–3971.
- (80) Wang, W.-N.; An, W.-J.; Ramalingam, B.; Mukherjee, S.; Niedzwiedzki, D. M.; Gangopadhyay, S.; Biswas, P. *J. Am. Chem. Soc.* **2012**, *134*, 11276–11281.
- (81) Koppenol, W. H.; Rush, J. D. *J. Phys. Chem.* **1987**, *91*, 4429–4430.
- (82) Xi, G.; Ouyang, S.; Ye, J. *Chem. - Eur. J.* **2011**, *17*, 9057–9061.
- (83) Abou Asi, M.; He, C.; Su, M.; Xia, D.; Lin, L.; Deng, H.; Xiong, Y.; Qiu, R.; Li, X.-z. *Catal. Today* **2011**, *175*, 256–263.
- (84) Xie, Y. P.; Liu, G.; Yin, L.; Cheng, H.-M. *J. Mater. Chem.* **2012**, *22*, 6746–6751.
- (85) Zhang, Q.; Gao, T.; Andino, J. M.; Li, Y. *Appl. Catal., B* **2012**, *123–124*, 257–264.